Article:
Simoni, M., Woo, C.L., Zhao, H. et al. (5 more authors) (2023) Reaction mechanisms, kinetics, and nanostructural evolution of magnesium silicate hydrate (M-S-H) gels. Cement and Concrete Research, 174. 107295. ISSN: 0008-8846

https://doi.org/10.1016/j.cemconres.2023.107295

Cement and Concrete Research 174 (2023) 107295

Contents lists available at ScienceDirect

Cement and Concrete Research

journal homepage: www.elsevier.com/locate/cemconres

Reaction mechanisms, kinetics, and nanostructural evolution of magnesium silicate hydrate (M-S-H) gels

Marco Simoni [a], Chun Long Woo [b], Han Zhao [b], Dinu Iuga [c], Petr Svora [d], Theodore Hanein [b,*], Hajime Kinoshita [b,*], Brant Walkley [a,*]

[a] Department of Chemical and Biological Engineering, University of Sheffield, S1 3JD, United Kingdom
[b] Department of Materials Science & Engineering, University of Sheffield, S1 3JD, United Kingdom
[c] Department of Physics, University of Warwick, Coventry, UK
[d] Department of Materials Engineering and Chemistry, Czech Technical University in Prague, Prague, Czech Republic

ARTICLE INFO

Keywords:
Magnesium silicate hydrate
Cement
M-S-H
Alternative cement
Kinetics
Microstructure
Nanostructure
Phase evolution

ABSTRACT

M-S-H gels were synthesised via reaction of $Mg(OH)_2$ with silica fume, cured at 35 °C for up to 112 days, and their chemical and nanostructural evolution was examined. M-S-H gels with structural similarity to the thermodynamically stable serpentine-group mineral lizardite were formed. Quantification of ^{25}Mg and ^{29}Si MAS and $^{1}H—^{29}Si$ CPMAS NMR, electron microscopy, and thermogravimetric data showed dissolution of brucite and silica fume, and M-S-H formation, all occurred linearly with time up to 56 days. Data showed strong correlation with the Avrami-Erofeyev nucleation kinetic model, indicating M-S-H formation was governed by nucleation reactions. After 112 days, two distinct M-S-H gels were formed: a Si-rich M-S-H gel with molar Mg/Si = 0.55(±0.2), and a Mg-rich M-S-H gel with molar Mg/Si = 0.80(±0.5). Nanostructural rearrangement of M-S-H continues up to 112 days, with increased crosslinking and polymerisation. This new insight is important for application of M-S-H binders in both construction and radioactive/toxic waste immobilisation.

1. Introduction

Magnesium-based cements are alternative low-carbon cements comprising predominantly a magnesium silicate hydrate (M-S-H) gel [1], and are typically formed by reaction of MgO or $Mg(OH)_2$ with a source of amorphous, reactive silica, in the presence of water. Magnesium-based cements have received growing interest recently, due to the low pH generated upon their hydration (9.5–10.5) [2] to form M-S-H gels, which is suitable for several applications, including the immobilisation of contaminants [3] and radioactive waste [4]. This pH range is lower than that found in other common cements (e.g. Portland-base and alkali-activated cements, among others), and is known to reduce the solubility of heavy metals [5] and hinder their dissolution, limiting their mobility. Therefore, magnesium-based cements comprising M-S-H gels exhibit strong potential as cement encapsulants for the long-term immobilisation of radioactive and toxic waste. On the other hand, such a low pH, relative to other common cements, would lead to depassivation of steel reinforcement [6] in concrete, potentially limiting the application of magnesium-based cements in construction. However, due to the expansive properties of M-S-H it has been suggested that optimum partitioning of M-S-H gels with conventional Portland cement (PC) would prevent long-term shrinkage-induced failure [7].

The main impediment for widespread implementation of M-S-H binders is the scarce and region-specific availability of natural $MgCO_3$ [8], from which MgO or $Mg(OH)_2$ are obtained upon calcination below 750 °C through the so-called 'dry route'. However, recent technological advances allow for the extraction of $Mg(OH)_2$ from more abundant magnesium silicates at lower temperatures [9,10], mitigating to some extent the scarcity issue. Alternatively, the 'wet route' is used for the synthesis of $Mg(OH)_2$ from magnesium present in seawater (around 1.3 g/L [11]). This process involves first deboration via use of ion-exchange resins, the subsequent removal of sulfates through addition of $CaCl_2$ and precipitation of $CaSO_4{\cdot}H_2O$, and finally reaction of the Mg-rich brine with $Ca(OH)_2$ to obtain $Mg(OH)_2$. This route also mitigates to some extent the scarcity of natural $MgCO_3$, but it is an energy-intensive process with several chemical processing steps required [12]. The potential use of radioactive $Mg(OH)_2$-rich Magnox waste is also very attractive, since it could lead to the synthesis of M-S-H cements with high waste

* Corresponding authors.
E-mail addresses: t.hanein@sheffield.ac.uk (T. Hanein), h.kinoshita@sheffield.ac.uk (H. Kinoshita), b.walkley@sheffield.ac.uk (B. Walkley).

https://doi.org/10.1016/j.cemconres.2023.107295
Received 30 March 2023; Received in revised form 21 July 2023; Accepted 1 August 2023
Available online 29 August 2023

Table 1
Oxide composition (wt%) of silica fume as determined by X-ray fluorescence analysis, together with the Loss On Ignition (LOI) at 1000 °C.[a]

Oxide	SiO_2	K_2O	MgO	Fe_2O_3	Al_2O_3	Na_2O	CaO	ZnO	Others	LOI (%)
Wt%	94.4	1.1	0.7	0.6	0.5	0.3	0.2	0.2	2.0	1.82

[a] Only compounds with >0.1 wt% are presented.

loading for radioactive waste disposal applications [13].

M-S-H is the main reaction product formed by hydration of MgO and/or $Mg(OH)_2$ with a source of silica [14]. M-S-H was initially identified as a degradation product of hardened Portland cement (PC) in chemically aggressive environments [15], and further investigation revealed that M-S-H is capable of providing strength when hardened, and exhibits good performance as a binder. M-S-H gels do not exhibit long range order, and are believed to be composed of tetrahedral and octahedral sheets containing mainly Si^{4+} and Mg^{2+}, respectively, and are often compared to talc ($Mg_3Si_4O_{10}(OH)_2$) or serpentine-group minerals ($Mg_3(Si_2O_5)(OH)_4$) [16–18]. However, there remains some debate around the most appropriate structural model for M-S-H [19]. For instance, Walling et al. suggested that M-S-H might largely consists of a poorly crystalline serpentine-like assembly, with the lizardite polymorphic structure [20], whereas Tonelli et al. reported "talc-like" and "chrysotile-like" [21], where chrysotile is a polymorph of lizardite.

It is also known that the chemical composition of M-S-H changes over its lifetime [22] and may depend on factors such as chemical composition of the precursors and reaction mixture, temperature, pressure, and activity of water. Such changes in chemical composition under different conditions, which are likely to then induce changes in the nanostructure of the gel, may also contribute to the difficulty in identifying its structural model; the reported Mg/Si molar ratio in M-S-H ranges from 0.57 to 1.3 [14,18,22]. It is also known that the formation of M-S-H cement is slow [23], limiting its use in certain applications where fast setting is required. Our previous study, however, showed that it is possible to accelerate M-S-H formation through the addition of water-soluble alkali carbonates [23], allowing tailored control of reaction kinetics.

In this study, we synthesise M-S-H gels via reaction of $Mg(OH)_2$ and silica fume, and use ^{25}Mg and ^{29}Si MAS NMR and $^{1}H—^{29}Si$ CP MAS NMR spectroscopy experiments, complemented by X-ray diffraction (XRD), electron microscopy, and thermogravimetric measurements, to examine the chemical and nanostructural evolution of the M-S-H gels over time. Through quantification of the thermogravimetric and NMR data and associated spectral deconvolutions, and fitting data regarding dissolution and extent of reaction over time with the appropriate solid-state kinetic models, we reveal mechanisms and kinetics of M-S-H formation, and the chemical composition, nanostructure, and local hydration of these M-S-H gels.

2. Experimental methods

2.1. M-S-H synthesis

Samples were prepared in a single batch using solid, powdered, reagent grade chemicals magnesium hydroxide $Mg(OH)_2$ (brucite, Sigma-Aldrich, ≥95 %) and silica fume (SiO_2, Elkem microsilica 940-U). $Mg(OH)_2$, rather than the more commonly used solid precursor MgO, was used as a precursor for the synthesis of M-S-H gel for two reasons: 1) the use of $Mg(OH)_2$ would be beneficial for commercialisation of M-S-H cements, given the alternative production routes cited above which would mitigate the limited availability of natural $MgCO_3$ required for production of MgO [9–11], and 2) $Mg(OH)_2$ powder facilitates faster dissolution of the solid precursor than MgO, and hence greater availability of soluble Mg^{2+} during the early stages of reaction. Due to differing precursor characteristics, and consequently differing rates of reaction, the findings discussed in this study should therefore be compared with those in studies that used MgO as a precursor for M-S-H synthesis within this context. The oxide (wt%) chemical composition of silica fume, as determined by X-ray fluorescence (XRF) analysis, is reported in Table 1, and the purity of silica fume is 94.4 % wt% SiO_2. Particle size distribution (PSD) analysis was performed using a Malvern Mastersizer, and revealed average diameter sizes (D_{50}) of 83.0 and 6.0 μm for the silica fume and brucite, respectively (Supplementary Information Fig. S1).

Samples were prepared in a single batch with mass ratios of $Mg(OH)_2$:silica fume:H_2O equivalent to 1:1:2, with excess distilled water provided to ensure a workable viscosity and complete hydration. Considering the purity of both $Mg(OH)_2$ and silica fume, this formulation resulted in a Mg/Si molar ratio of 1.05 for all samples. The batch was mixed in ambient conditions initially for 2 min using a Kenwood benchtop planetary mixer at speed 1 (~150 rpm) by first adding the distilled water to the brucite powder, and then adding silica fume slowly over 2 min to avoid dusting and mass loss. Once all the silica fume was added, the batch was mixed in the same Kenwood planetary mixer for a further 5 min, and subsequently mixed for a further 5 min using a Heidolph high-shear overhead stirrer at 800 rpm to produce a homogeneous paste. The paste was then divided into five 50 mL centrifuge tubes (each approximately 30 mL filled) which were sealed using standard centrifuge tube caps and cured at 35 °C in an environmental chamber (without control of the relative humidity) for 7, 14, 28, 56, and 112 days.

After curing, the samples were immersed in acetone and gently stirred for 5 min. The acetone-solid mixture was then filtered using a vacuum assisted Büchner funnel with filter paper (Whatman, Grade 1, 90 mm) for 10 min. The samples were then immersed in fresh acetone in a sealed container for 48 h to arrest the hydration process. Finally, the mixtures were again filtered for 15 min using a vacuum assisted Büchner funnel with filter paper (Whatman, Grade 1, 90 mm), and dried for 5 min under ambient conditions. The dried M-S-H samples were then broken and stored in sealed containers for characterisation. For all analyses, except scanning electron microscopy (SEM), the samples were manually ground into powder using an agate mortar and pestle for 2 min, and subsequently sieved below 63 μm using a standard US 230 mesh steel sieve.

2.2. Sample characterisation

2.2.1. X-ray fluorescence (XRF)

A Claisse LeNeo Fluxer was used to prepare a sample bead, and X-ray fluorescence (XRF) measurements were performed on a PANalytical Zetium instrument, operated with PANalytical SuperQ software. The PANalytical WROXI (wide-ranging oxides) calibration was used to determine the oxide composition in weight %, assuming simple oxides from the elements. The fused 40 mm bead used for measurements was made by mixing 10 g of lithium tetraborate (with 0.5 % LiI) flux with 1 g of sample. The pre-mixed sample and salt was heated in five steps, in a platinum crucible, prior to being poured and cooled: a) 4 min at 1065 °C, b) 3 min at 1065 °C while rocking at 10 rpm and an angle of 15°, c) 6 min at 1065 °C rocking at 30 rpm and an angle of 40°, d) 1 min at 1000 °C, and e) 4 min at 1000 °C rocking at 25 rpm and an angle of 45°. Three measurements were taken on the same bead, and the average values recorded.

2.2.2. X-ray diffraction (XRD)

X-ray diffraction measurements were performed using a Bruker D2 PHASER diffractometer in the Bragg-Brentano geometry equipped with a Cu-Kα radiation source running at 30 kV and 10 mA. The powdered

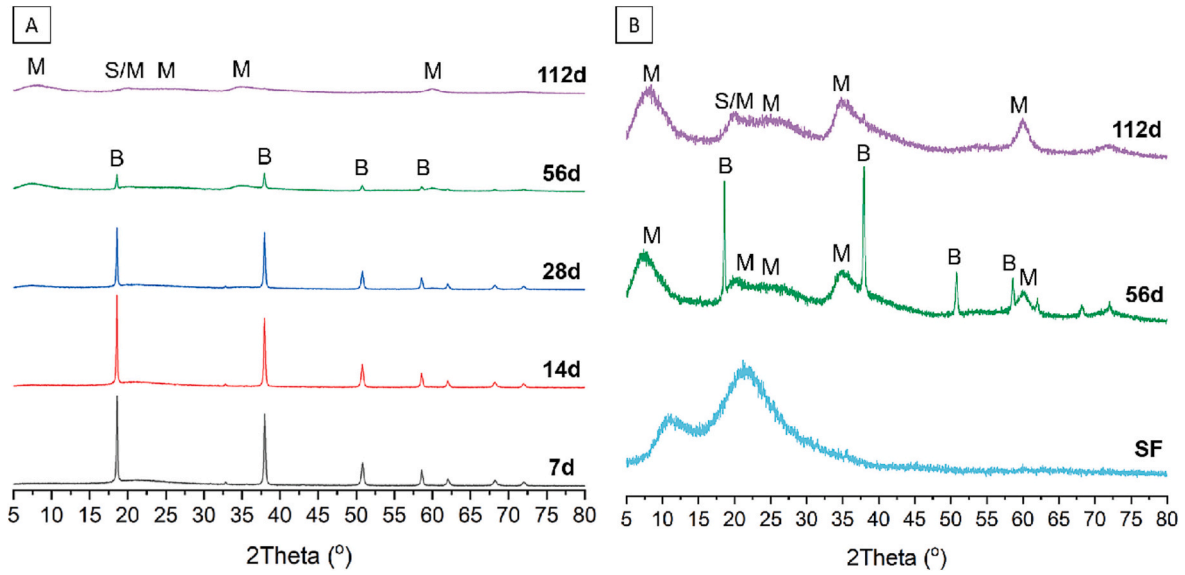

Fig. 1. (A) XRD data for samples cured for 7, 14, 28, 56, and 112 days. (B) XRD data for samples cured for 56 and 112 days, as well as silica fume, with the vertical axis rescaled (c.f. that in A)) to highlight the broad features attributed to M-S-H. Diffraction peaks attributed to M-S-H gel are marked with M, brucite with B and silica fume with S. Note that the features attributed to M-S-H are only observed in the XRD data for samples cured for 56 and 112 days.

sample was back-loaded onto a steel sample holder with a 15 mm diameter exposed area. The 1 mm primary divergence slit was used with the 3 mm air scatter screen module. X-ray patterns were collected in the range of 5–80° 2θ at 0.02° increments and 0.4 s per step. The lower and upper discriminator settings were 0.11 V and 0.25 V respectively. Samples were rotated at 30 rpm; nickel and K filter were both fitted. The XRD patterns obtained were indexed using Bruker DIFFRAC.EVA software furnished with the PDF-4+ 2020 database.

2.2.3. Scanning electron microscopy (SEM) with energy dispersive X-ray spectroscopy (EDS)

Microphotography and determination of elemental chemical composition was performed on a high-resolution Zeiss FEG SEM Merlin scanning electron microscope, using an AsB detector for imaging and an X-MaxN 150 energy-dispersive spectrometer (EDS) for elemental analysis, with AZtec 3.1 SP1 software. Spatially-resolved SEM-EDX data for all samples was obtained using a magnification, working distance and voltage of 1000, 8.5 mm and 20 kV, respectively. Visual observation of the EDX spectra for each sampling point showed that for all spectra the signal/noise ratio was sufficiently high that the noise could be considered negligible relative to the signal. EDX data were post processed within free timed licensed AZtec 4.3, and the EDX data points were normalised so that the sum of all elements observed at a single point equalled 100 mol%. An evenly distributed selection of EDX data points across a representative 400 μm × 400 μm section of the sample were acquired for all samples, and subsequently analysed using an ordinary one-way ANOVA with Tukey's multiple comparisons test, performed using GraphPad Prism 9 (version 9.5.1).

Microscopic cross-sections were made from the cement samples. Before making the cross-section, it was necessary to fill the pore space with a suitable substance to avoid loosening the grains of materials during sample preparation. Vacuum impregnation of samples with epoxy resin (Struers EpoFix kit) was used for this purpose. The cross-sections were prepared on a Tegramin machine from Struers. Samples were ground and polished in multiple steps to achieve the best surface quality of the samples. In the first step, 220 grain/cm^2 SiC grinding foil was used to remove the greatest irregularities after cutting. In the next steps, finer SiC foils were used: 500 grain/cm^2, 1200 grain/cm^2, 2000 grain/cm^2, and 4000 grain/cm^2. Each step lasted 4 min with a pressure of 5 N. The entire sample preparation was performed using a dry method, without water. Samples were then coated with a conductive carbon coating prior to analysis.

2.2.4. Thermogravimetry (TG)

Thermogravimetric analysis data were acquired using a PerkinElmer TGA 4000. Approximately 40 mg of powder sample was heated from 30 °C to 990 °C at a rate of 10 °C per minute with a nitrogen flow of 40 mL per minute. An isothermal hold was also applied at the start and end temperatures for 5 min.

2.2.5. Solid state nuclear magnetic resonance (NMR) spectroscopy

Solid state single pulse ^{29}Si magic angle spinning (MAS) NMR data were acquired on a Bruker Avance III HD 500 spectrometer at 11.7 T (B_0) using a 4.0 mm dual resonance cross-polarisation (CP) MAS probe, yielding a Larmor frequency of 99.35 MHz. ^{29}Si MAS NMR spectra were acquired using a 5.5 μs non-selective (π/2) excitation pulse, a measured 60 s relaxation delay, a total of 256 scans and spinning at 12.5 kHz. ^{1}H—^{29}Si CP MAS NMR experiments were performed using the same instrument with a spinning frequency of 12.5 kHz, a ^{29}Si non-selective (π/2) pulse width of 5.5 μs, an initial ^{1}H non-selective (π/2) pulse width of 2.5 μs, a recycle delay of 0.5 s and Hartmann-Hahn contact periods of 2 and 8 ms. A nominal ^{1}H decoupling field strength of 80 kHz was employed during acquisition and 2048 scans were collected per experiment. All ^{29}Si spectra were referenced to pure tetramethylsilane at 0 ppm.

Gaussian peak profiles were used to deconvolute the ^{29}Si MAS and ^{1}H—^{29}Si CP MAS NMR spectra [24]. The minimum number of peaks possible were fitted, and the isotropic chemical shift (δ_{iso}) and peak full width at half maximum (FWHM) of each resonance were required to be consistent in both the ^{29}Si MAS NMR and ^{1}H—^{29}Si CP MAS NMR spectral deconvolution. In all deconvolutions, congruent dissolution of Si sites in silica fume was assumed and the contribution from unreacted silica particles was considered by fitting a scaled component spectrum calculated from that of silica fume.

High-field solid state single pulse ^{25}Mg MAS NMR data were acquired at the UK 850 MHz solid-state NMR Facility on a Bruker NEO 850 spectrometer at 20.0 T (B_0) yielding a Larmor frequency of 52.04 MHz, using a 4.0 mm MAS probe, spinning at 14 kHz. ^{25}Mg MAS NMR spectra were acquired using an echo sequence with a 2.5 μs (π/2) and 5 μs (π) non-selective pulses with one rotor period echo time, a total of 84,000

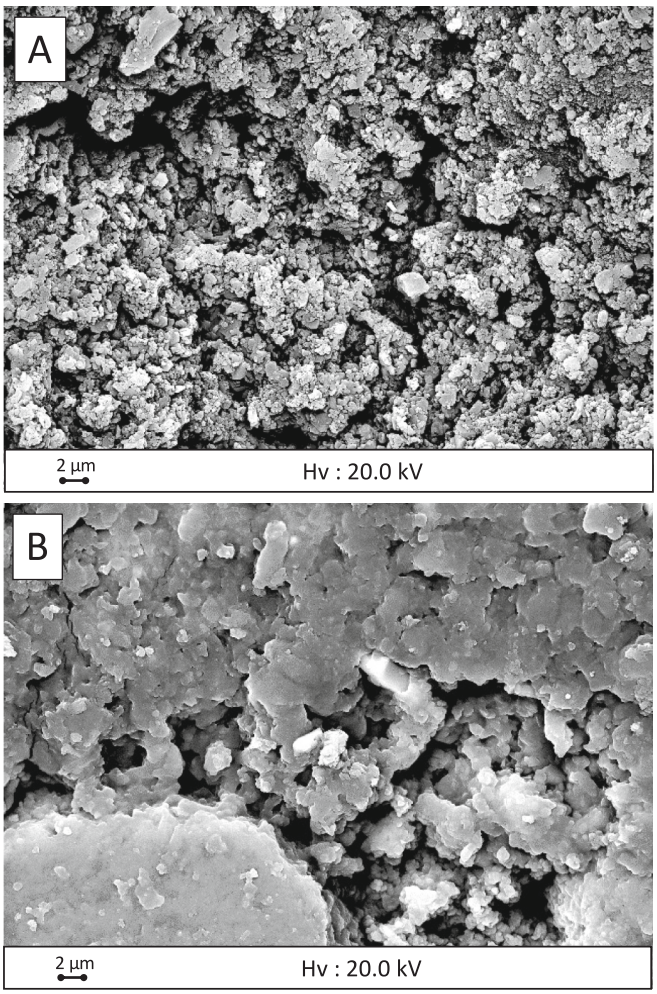

Fig. 2. Secondary electron SEM images of the samples cured for A) 7 and B) 112 days. At 7 days, mostly unreacted silica fume and brucite are shown. At 112 days the non-rigid structure of the produced M-S-H can be observed.

scans were acquired with 1 s relaxation delay. A double frequency sweep was used before the echo sequence, to increase the polarisation of the central transition [25]. All ^{25}Mg MAS NMR spectra were referenced to MgO at 26 ppm. ^{25}Mg lineshapes were simulated in MATLAB using the second-order quadrupolar lineshape [26]. The disorder in the samples were simulated considering a Gaussian distribution of the Quadrupole coupling constant as well as a Gaussian distribution in isotropic chemical shift.

3. Results and discussion

3.1. Qualitative analysis of phase assemblage and microstructural evolution

The discussion presented here focuses on the reaction of the two main components in the precipitated M-S-H gel, Mg and Si, and the effect of their availability on the composition and structure of the M-S-H gel formed, upon dissolution of brucite and silica fume. XRD analysis was used to monitor evolution of the phase assemblage of the samples over the time. The XRD patterns of all samples are reported in Fig. 1A, with diffraction peaks marked M, S, and B identifying signals from M-S-H gel [27], silica fume [27] and brucite (PDF no. 04–011-5938), respectively.

Fig. 1B shows the XRD patterns for samples cured for 56 and 112 days, as well as silica fume, rescaled to highlight the signals due to

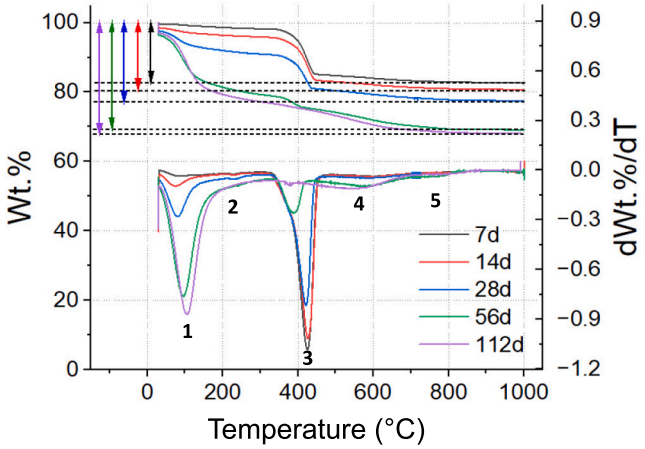

Fig. 3. TG/dTG trends of the samples discussed, cured for 7, 14, 28, 56, and 112 days. Mass loss event 1, 4, and 5 are attributed to M-S-H, and mass loss events 2 and 3 are attributed to brucite.

diffuse scattering that is characteristic of the presence of an M-S-H gel. Complete dissolution of brucite does not occur until 112 days of curing, with the main reflection attributed to brucite at 18.7° 2θ persisting until 56 days after initial hydration, indicating incomplete reaction of brucite in these samples. Previous authors [28,29] have reported X-ray data for M-S-H within 5–70° 2θ exhibiting broad features due to diffuse scattering at 10–13°, 20–22°, 24–27°, 35–39° and 60–62° 2θ. These broad features are commonly attributed to disordered M-S-H gels. Previous work [28] has also shown that the broad feature at 10–13° 2θ can shift to 5–6° 2θ, possibly due to the enlargement of the interlayer distances or the nano-crystallinity of the M-S-H [30].

The broad features in the XRD data shown in Fig. 1 for the sample produced here are in good agreement with those reported in the literature [28,29], and indicate that the consumption of brucite, in the presence of silica fume, leads to the formation of an M-S-H gel. The features in the XRD data attributed to the M-S-H gel gradually increase in intensity with increasing curing time, in line with the consumption of brucite and the higher availability of Mg^{2+} ions, and consequent increased formation of the M-S-H gel.

Overall, the XRD data suggest that the consumption of brucite (and hence the expected subsequent precipitation of M-S-H gel) occurred only after 28 days of hydration (Fig. 1A). Formation of M-S-H is, however, observed as early as 7 days curing by other characterisation techniques used in this study, as evidenced by TG-MS, SEM and solid-state NMR data discussed below, but is not observable by XRD before 56 days. Finally, it should be noted that the broad feature detected for M-S-H at 20–22° 2θ overlaps with the characteristic broad feature of silica fume at 18–25° 2θ, also reported in Fig. 1B. Together, these aspects highlight the limitations of using solely XRD data to identify formation of M-S-H gels, and the necessary use of both spectroscopic and thermogravimetric characterisation techniques to identify this phase, as discussed below.

Phase and microstructural evolution of these samples occurring between 7 and 112 days of curing may be observed further in the secondary electron micrographs of fracture surfaces obtained by SEM and reported in Figs. 2A and 2B, respectively. After 7 days of curing, the system was primarily composed of unreacted silica fume and brucite (Fig. 1A) embedded within a dense M-S-H gel; the lamellar-like brucite crystals could be observed in Fig. 2A. Over time, the dissolution of both brucite and silica fume led to the disappearance of the irregular fractures shown in Fig. 2A, to give a smoother structure with a significantly higher apparent gel density after 112 days of curing (Fig. 2B). M-S-H exhibited a gel-like morphology with globular chains, consistent with previous observations [21].

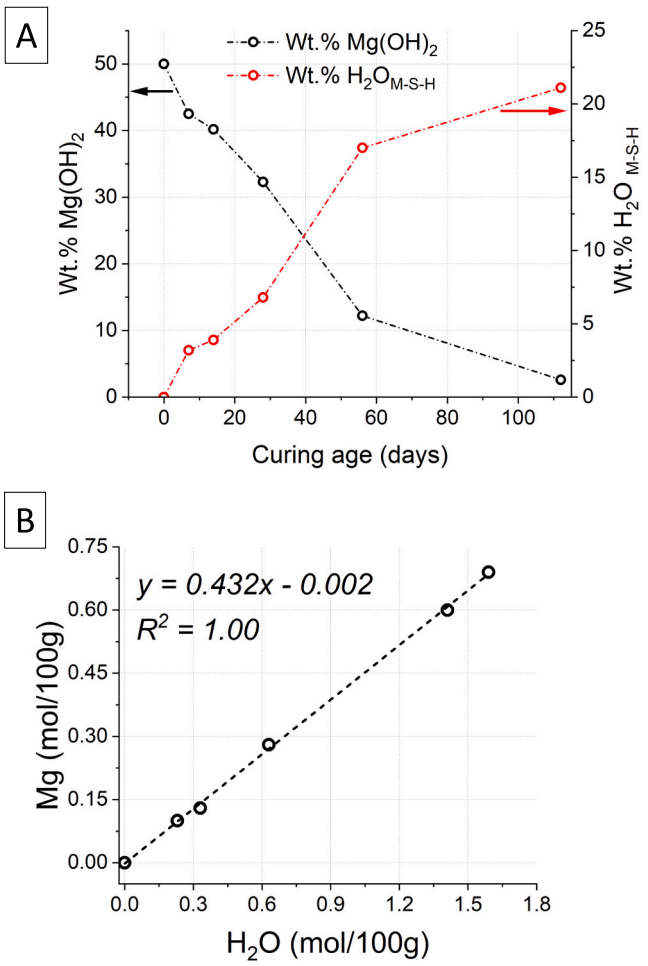

Fig. 4. Estimated residual $Mg(OH)_2$ and M-S-H water in samples cured for 7, 14, 28, 56, and 112 days (black circles, from left to right). The points at 0 days are not measured but assumed.

3.2. *Quantification of reaction of brucite ($Mg(OH)_2$) and formation of M-S-H*

Starting from these qualitative observations, thermogravimetric (TGA) analysis aimed to quantify the extent of dissolution of brucite to highlight the correlation with the precipitation of M-S-H. Overall, five mass loss events were observed during heating (labelled in Fig. 3), with each indicating the behaviour of brucite and M-S-H in the temperature ramp set up.

Overall, increasing weight losses were observed at longer curing ages (17.5, 19.4, 22.5, 30.9 and 31.7 wt% at 7, 14, 28, 56 and 112 days, respectively). This indicated an increasing reaction extent (i.e. formation of more M-S-H gel) and reduction in the amount of brucite in the samples (Fig. 1A), whose weight loss events could be observed around 200–250 °C (2) and 350–450 °C (3) [31]. Specifically, while the former temperature range referred to the evaporation of adsorbed water on the surface of brucite, the latter comprised two overlapping weight loss events with maximum at 380 °C and 425 °C. These were due to the dehydroxylation of brucite in two stages, which Nahdi et al. observed to be a result of formation of an intermediate phase with hexagonal geometry below 400 °C, which would finally decompose around 430 °C [32].

Quantification of brucite can be performed by considering the overall weight loss in (3), which was distinct and therefore reliably quantifiable for all the samples except for that cured for 112 days. However, the weak intensity of the weight loss at 382 °C suggested that brucite was a minor phase after 112 days of curing. The weight losses linked to M-S-H could be observed at 80–200 °C (1), 500–550 °C (4) and above 700 °C (5) (Fig. 3), and the quantification of the water linked to M-S-H could be obtained upon sum of the signals (1, 4, 5) specifically adjusted for each sample considered. The loss of molecular and coordinated water from M-S-H (i.e. dehydroxylation of the Mg-OH groups in M-S-H) [33,34] occurred in (1, 4), respectively; the further loss in (5) was likely reflecting the dehydroxylation of the inner Mg-OH groups occurring at higher temperatures [35]. Such signal was evident only for the samples cured for 56 and 112 days, and it was possibly identifying an enhanced incorporation of Mg within M-S-H over time.

Overall, in accordance with the XRD analysis (Fig. 1A), the brucite

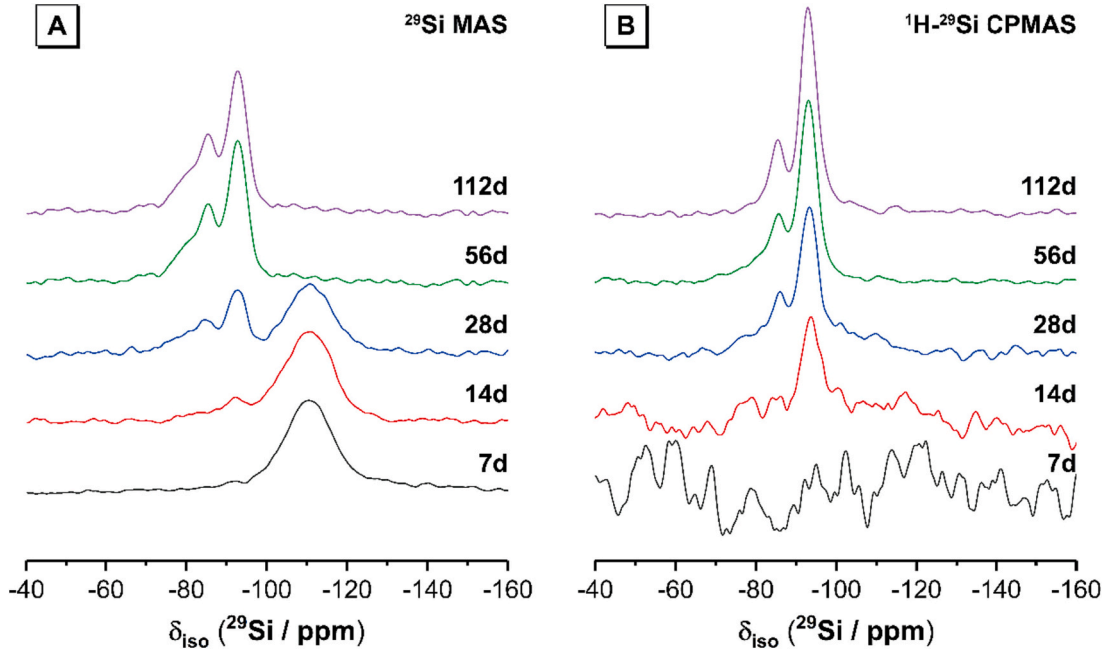

Fig. 5. A) ^{29}Si MAS ($B_0 = 11.7$ T, $\nu_R = 12.5$ kHz) NMR and B) ^{1}H—^{29}Si CPMAS ($B_0 = 11.7$ T, $\nu_R = 12.5$ kHz, Hartmann-Hahn contact period $t = 8$ ms) NMR spectra of samples cured for 7, 14, 28, 56 and 112 days as marked.

Table 2
Isotropic chemical shift (δ_{iso}) and the full width at half maximum (FWHM) extracted from the deconvoluted ^{29}Si MAS NMR spectra (Fig. 7). δ_{iso} and FWHM were required to be consistent in both the ^{29}Si MAS and ^{1}H—^{29}Si CPMAS NMR spectra.

Parameter	Q^1	Q^2	Q^3(I)	Q^3(II)	Q^4
δ_{iso} (ppm)	−79.0	−85.4	−93.0	−99.0	−110.5
FWHM (ppm)	8.0	4.9	5.0	8.0	13.5

content in the samples decreased approximately linearly with increasing curing time, whereas an opposite trend was observed for the M-S-H (Fig. 4A). Such trends suggested that the rate determining step for the formation of M-S-H is the availability of Mg^{2+} ions, since the trends reported in Fig. 4A are complementary.

The dissolution of brucite occurs predominantly between 28 and 56 days of curing (over 40 wt%, Fig. 4A), therefore providing more Mg to be incorporated within the M-S-H structure, however this is likely a result of the significantly larger interval between these two time points, in comparison to other time intervals. Interestingly, the rate of brucite consumption is approximately constant from the beginning of reaction to 56 days of curing, and then drops to about 25 % of that initial rate. This is likely due to reduced availability of free water that is required for further dissolution of brucite, as well as steric hindrance resulting from precipitation of M-S-H, which would reduce the free space into which additional M-S-H could precipitate.

The Mg^{2+} available for the precipitation of M-S-H, reported as mol/100 g in Fig. 4B, was obtained via a mass balance of brucite. The linear correlation between this value and the water bound to the M-S-H formed suggested a stoichiometric relationship between the Mg^{2+} made available upon dissolution of brucite and the M-S-H formed; it was calculated that 2.3 molecules of water were incorporated into M-S-H for each Mg ion made available upon dissolution of brucite, on average over 112 days of curing. Finally, the weight loss reported after 56 and 112 days of curing only could possibly be linked to a further incorporation of Mg within the M-S-H, leading to a modification of the Mg/Si ratio of the gel phase, and therefore supporting the anomalous shift to 5–6° 2θ observed in the XRD patterns (Fig. 1B).

3.3. Solid state nuclear magnetic resonance spectroscopy

3.3.1. Nanostructural characterisation of M-S-H

The ^{29}Si MAS and ^{1}H—^{29}Si CPMAS NMR data for each sample (Fig. 5A and B, respectively) exhibit resonances at δ_{iso} = −79.0, −85.4, −93.0, −99.0 and − 110.5 ppm (spectral parameters are provided in Table 2).

The resonances at δ_{iso} = −79.0, −85.4, −93.0 and − 99.0 ppm are attributed to a Q^1 site, a Q^2 site and two distinct Q^3 sites (denoted Q^3(I) and Q^3(II)), respectively, within the M-S-H gel. These resonances are consistent with previous observations for disordered M-S-H [14,16,20,21,36–39]. The resonance at δ_{iso} = −110.5 ppm, observed prominently in the younger samples, corresponds to Q^4 sites within unreacted silica fume [40–42]. The main component of the ^{29}Si MAS NMR spectra attributed to the formation of M-S-H gel is the Q^3(I) resonance, and its chemical shift (δ_{iso} = −93.0 ppm) is consistent with that of the Q^3 resonance in the serpentine-group minerals (polymorphs of $Mg_3(Si_2O_5)(OH)_4$) chrysotile [43], lizardite [20] and antigorite [44,45], while the chemical shift of the lower intensity Q^3(II) resonance (δ_{iso} = −99.0 ppm) is consistent with that of the Q^3 resonance in talc ($Mg_3Si_4O_{10}(OH)_2$) [46], albeit somewhat broader due to the local disorder of this site such as structural deformation [30] or branching silicate chain sites [29]. The high degree of Q^3 sites relative to Q^2 and Q^1 sites indicates a significant degree of polymerisation in the M-S-H gel.

In this study, the resonance at δ_{iso} = −110.5 ppm is attributed to Q^4 sites within unreacted silica fume [40–42] as mentioned above. Some previous work has attributed a resonance within this region of the ^{29}Si MAS NMR spectrum to Q^4 sites within a M-S-H gel, however this does not align with the NMR data of talc [21] or serpentine-group minerals [20], nor the bulk of previously published work on M-S-H gels [14,16,20,21,36–39]. The intensity of resonances in ^{1}H—^{29}Si CPMAS NMR data is modulated by their proximity to protons and the Hartmann-Hann contact period (discussed in further detail below), and consequently this spectrum indicates more prominently those Si species that are within the hydrated reaction product. The ^{1}H—^{29}Si CPMAS NMR data in Fig. B confirm that the broad resonance at δ_{iso} = −110.5 ppm identified in the ^{29}Si MAS NMR results (Fig. 5A) is attributable to the anhydrous Q^4 Si sites present in unreacted silica fume particles, as it is absent from the CPMAS spectra.

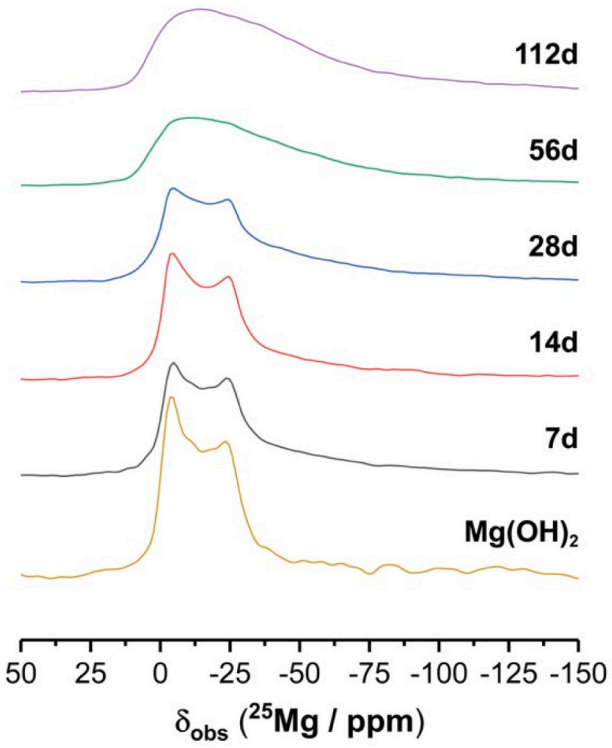

Fig. 6. High field ^{25}Mg MAS (B_0 = 20.0 T, ν_R = 14.0 kHz) NMR spectra of brucite ($Mg(OH)_2$) and samples cured for 7, 14, 28, 56 and 112 days as marked.

To further understand the dissolution of brucite and contribution of Mg to the formation of M-S-H at longer curing ages, high-field (20.0 T) solid state ^{25}Mg MAS NMR data were acquired for each sample, as well as pure brucite ($MgOH)_2$) (Fig. 6).

The ^{25}Mg MAS NMR spectrum for brucite is well characterised within the literature, and at this field strength exhibits a resonance with a split double peak due to strong second-order quadrupolar interactions of the central transition due to Mg in a single distorted octahedral site [47], with δ_{iso} values reported to be between −10.0 ppm and − 14.1 ppm [48–50]. This is consistent with the ^{25}Mg MAS NMR spectrum for brucite in the work presented here, which exhibits a resonance with δ_{obs} = −13.0 ppm.

The ^{25}Mg MAS NMR spectrum of the M-S-H sample cured for 7 days exhibits a resonance with a line shape very similar to that of brucite, indicating that a significant proportion of unreacted brucite is present within the sample. Additional intensity is also observed between −40 and − 80 ppm, indicating formation of a phase containing significantly disordered octahedral Mg sites. The spectrum for M-S-H cured for 14 days is almost identical to that cured for 7 days, indicating little change in Mg environments, however as curing time is increased from 14 days

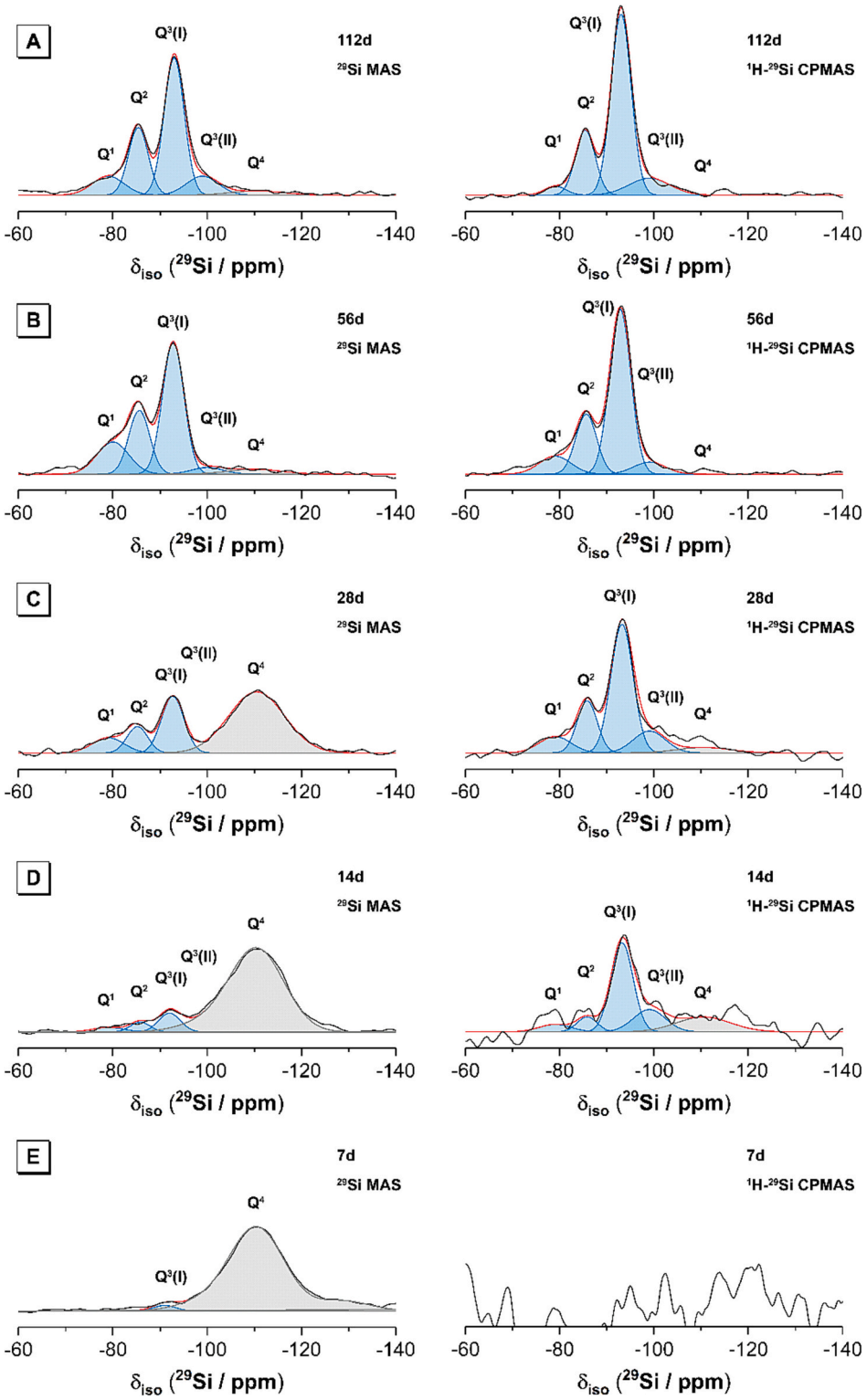

Fig. 7. ^{29}Si MAS ($B_0 = 11.7$ T, $\nu_R = 12.5$ kHz) and ^{1}H—^{29}Si CPMAS ($B_0 = 11.7$ T, $\nu_R = 12.5$ kHz) NMR data and associated deconvolutions for samples cured for 112 (A), 56 (B), 28 (C), 14 (D) and 7 (E) days. Data are shown in black; the fit (shown in red) is the sum of the deconvoluted peaks; peaks attributed to Si sites in M-S-H are shaded in blue; those attributed to sites within remnant anhydrous silica fume are shaded in grey. (For interpretation of the references to colour in this figure legend, the reader is referred to the web version of this article.)

to 112 days, the resonance attributed to octahedral Mg sites in unreacted brucite particles decreases, and a new broad resonance centred at $\delta_{obs} = -14.0$ ppm is observed in the ^{25}Mg MAS NMR spectrum of the M-S-H samples.

The resonance attributed to Mg sites in remnant brucite particles is not observed in the ^{25}Mg MAS NMR spectrum of the M-S-H cured for 112 days, consistent with the TG data discussed above that shows almost complete consumption of brucite after curing for 112 days. This spectrum exhibits a broad resonance spanning from $\delta_{obs} = -10.0$ ppm to -100 ppm, centred at $\delta_{obs} = -14.0$ ppm, indicating extensive disorder of the Mg sites. The position and line shape of this resonance is consistent with Mg sites within M-S-H gels exhibiting short range (approximately within the first and second coordination spheres) structural similarity to the serpentine-group mineral lizardite [20]. This contrasts with some other studies which have reported formation of M-S-H gels with structural similarity to the serpentine group minerals chrysotile

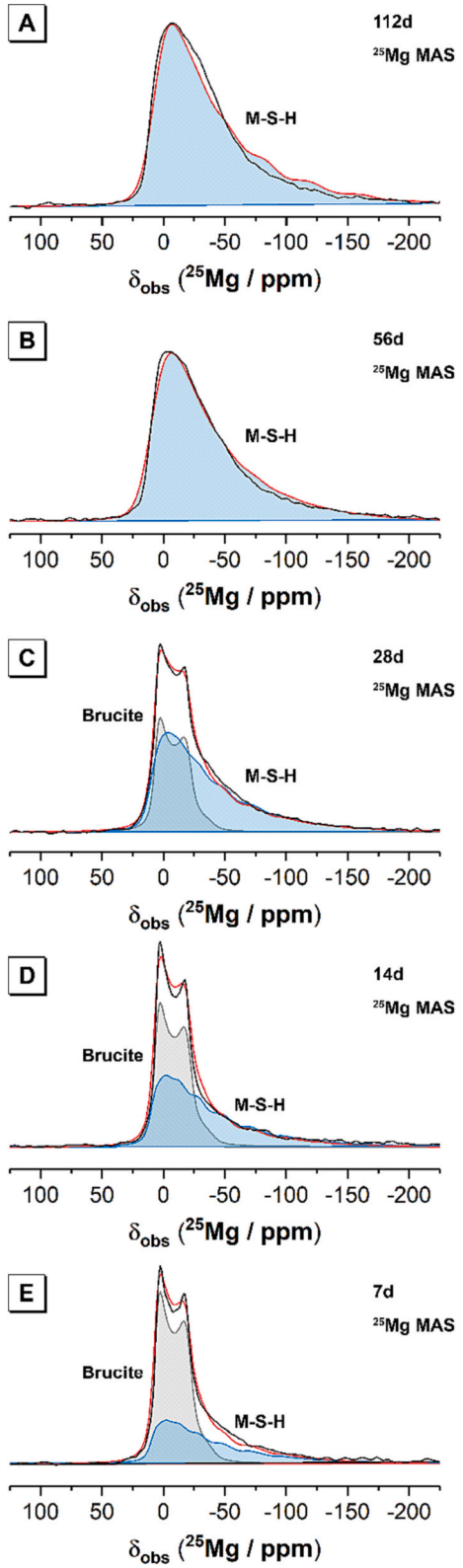

Fig. 8. ^{25}Mg MAS (B_0 = 20.0 T, ν_R = 14 kHz) NMR data and associated deconvolutions for samples cured for 112 (A), 56 (C), 28 (E), 14 (G) and 7 (I) days. Data are shown in black; the fit (shown in red) is the sum of the deconvoluted peaks; peaks attributed to Si sites in M-S-H are shaded in blue; those attributed to sites within remnant unreacted brucite are shaded in grey. (For interpretation of the references to colour in this figure legend, the reader is referred to the web version of this article.)

and antigorite [21].

Previous work by Vespa et al. [51] showed that M-S-H gels formed using MgO as a precursor exhibited a TOT phyllosilicate structure with silica defects creating end of silica chains, and an interlayer composed of Mg bound to hydroxide groups, with strong structural similarity to the aragonite and talc; work by Bernard et al. [52] also observed that M-S-H gels produced using MgO as a precursor exhibited structural similarity with talc. The differences in local structure to the M-S-H gels produced in those studies comparted with that observed in the study presented here using $Mg(OH)_2$ as a precursor likely arise to the different precursor used as a source of Mg, and consequent differences in availability of Mg and Si during reaction and curing.

Predictions from thermodynamic and kinetic data show that lizardite is the stable phase at temperatures below approximately 300 °C [53], with antigorite forming only at temperatures above approximately 250 °C [53] and chrysotile forming only from supersaturated solutions due to kinetic effects [54] (and being thermodynamically unstable in the M-S-H system [53]). Together, the ^{25}Mg MAS, ^{29}Si MAS, and ^{1}H—^{29}Si CPMAS NMR data discussed above indicate that the M-S-H gel exhibits greater structural similarity with the more thermodynamically stable phase lizardite, consistent with previous reasoning for M-S-H gels in similar systems [20]. This suggests that the thermodynamically stable phase in this system is formed within 112 days.

3.3.2. *Nanostructural development of M-S-H over time*

The ^{29}Si MAS NMR data (Fig. 7) shows a steady decrease in the intensity of the resonance attributed to Q^4 sites within unreacted silica fume ($\delta_{iso} = -110.5$ ppm) with curing time, while a steady increase is observed in the intensities of the resonances attributed to Q^1, Q^2, Q^3(I) and Q^3(II) sites within the M-S-H gel. This indicates continuous consumption of silica fume and formation of the M-S-H gel occurring prominently from 7 to 56 days. Similar, the ^{25}Mg MAS NMR data (Fig. 8) and associated spectral deconvolutions show a steady decrease in the intensity of the resonance attributed to octahedral Mg sites in brucite ($Mg(OH)_2$) ($\delta_{iso} = -13.5$ ppm, quadrupolar coupling constant, $Q_c = 3.0$ MHz) with curing time, while a steady increase is observed in the intensities in this data of the broad resonance attributed to Mg sites in the M-S-H gel ($\delta_{iso} = 6.0$ ppm, $Q_c = 4.2$ MHz). Full details of the NMR parameters obtained for each site via fitting the ^{25}Mg MAS NMR data are provided in Table S1, Supplementary Information.

Quantification of the ^{29}Si MAS NMR spectral deconvolutions (Fig. 9a) shows that these changes in intensity occur approximately linearly with time (within error of the quantification, ~ 1 mol%) up to 56 day of curing, aligning with the linear decrease of $Mg(OH)_2$ and linear increase of water in M-S-H in the samples with time observed by TG analysis (Fig. 3). Quantification of both the ^{29}Si MAS NMR and ^{25}Mg MAS NMR spectral deconvolutions (Fig. 8b) shows that both the decrease in Si and Mg sites in the NMR data for the precursors (silica fume and brucite, respectively) and the increase in Si and Mg sites in the NMR data for the M-S-H gels occurs approximately linearly with time up to 56 days of curing.

After this time, the consumption of silica fume and brucite and their incorporation of Si and Mg into M-S-H plateaus, but the nanostructural rearrangement of the M-S-H gel continues, with an increase of Q^3(II) sites and a decrease in Q^1 sites observed in the ^{29}Si MAS NMR data between 56 and 112 days. This indicates continued crosslinking and polymerisation of M-S-H as the gel ages. That is in accordance with the XRD (Fig. 1A) and TG (Fig. 3) data discussed above, which show continued consumption of silica fume and brucite and an increase in mass of water in M-S-H gel between 56 and 112 days. Together with the ^{29}Si MAS NMR data, this indicates continued incorporation of Mg into the M-S-H gel and an increase in the bulk gel Mg/Si ratio between 56 and 112 days, due to preferential formation of additional Mg-rich M-S-H phase in the sample (consistent with observations by SEM-EDX, discussed below).

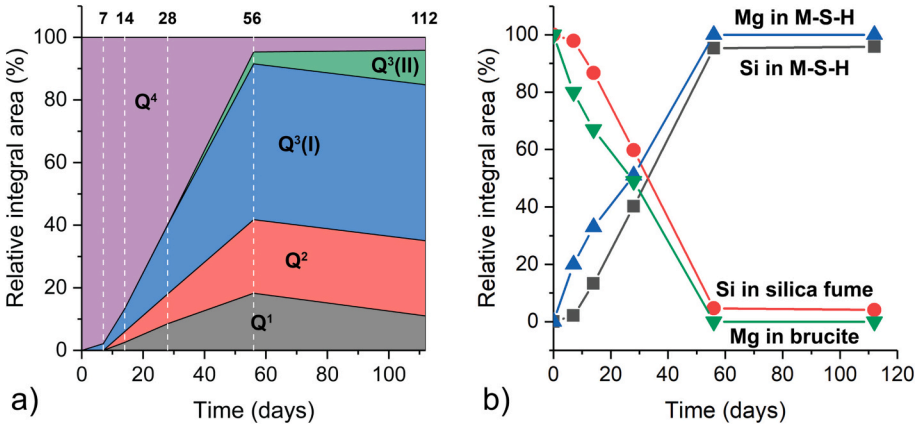

Fig. 9. a) Changes in relative integrated intensity (integral area normalised to the sum of all sites) with time in the ^{29}Si MAS NMR data; estimated error is 1 %. It is assumed that the only contribution to the ^{29}Si MAS NMR data at 0 days is from Q^4 sites in silica fume. b) Changes in the sum of all relative integrated intensities (integral area normalised to the sum of all sites) of Si and Mg sites in M-S-H, silica fume and brucite in the ^{29}Si and ^{25}Mg MAS NMR data. Si in M-S-H = Q^1+ Q^2+ Q^3(I) + Q^3(II); Si in silica fume = Q^4; Mg in M-S-H = broad Mg sites with similarity to Mg in lizardite; Mg in brucite = Mg sites with structural similarity to brucite.

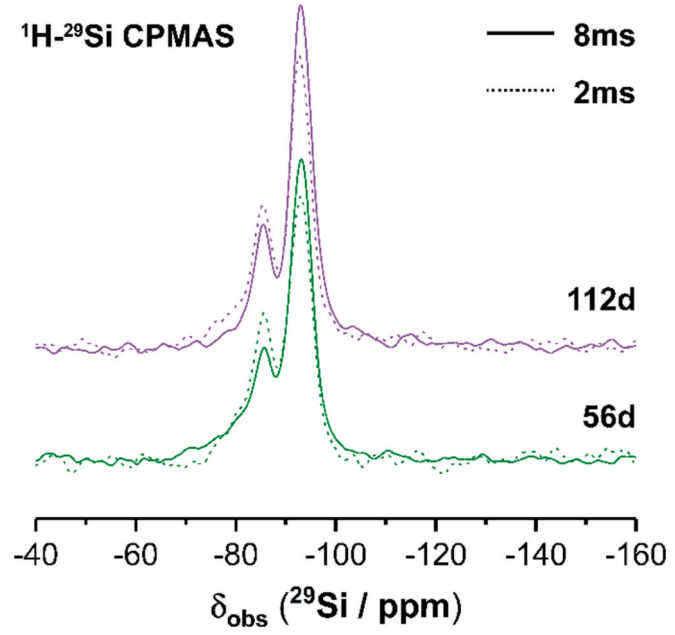

Fig. 10. ^{1}H—^{29}Si CPMAS (B_0 = 11.7 T, ν_R = 12.5 kHz) NMR spectra with Hartmann-Hahn contact periods of t = 2 and 8 ms of samples cured 56 and 112 days as marked.

3.3.3. *Changes in surface chemistry and local hydration of the M-S-H gel over time*

A further understanding of the local hydration of each Si site within the M-S-H gel was achieved through ^{1}H—^{29}Si CPMAS NMR run at different Hartmann-Hahn contact periods (t = 2 and 8 ms). Magnetisation transfer during cross polarisation depends on the strength of the ^{1}H—^{29}Si magnetic dipolar interaction; a stronger dipolar interaction will result in faster transfer of magnetisation. Thus, the intensity of resonances in ^{1}H—^{29}Si CPMAS NMR data is modulated by the proximity of Si nuclei to protons (the ^{1}H—^{29}Si internuclear distance) and the Hartmann-Hann contact period. Shorter contact periods will therefore preferentially enhance resonances of Si sites in closest proximity to protons (i.e. those that are most hydrated) and longer contact periods preferentially enhance resonances of Si sites which are further away from protons (i.e. those that are less hydrated). The comparison of the ^{1}H—^{29}Si CPMAS NMR data for M-S-H samples cured for 56 and 112 days (i.e. those comprising mostly M-S-H) was acquired using different Hartmann-Hahn contact periods, allowing for a deeper insight into the local hydration of each Si site within the M-S-H gel (Fig. 10).

The resulting quantification of the relative integral areas (%) Q^1, Q^2, Q^3(I), Q^3(II) and Q^4 is reported in Table 3 below. The results indicate that Q^2 sites within the M-S-H gel are in closest proximity to protons and hence exhibit the greatest degree of hydration, whereas the Q^1, Q^3(I) and Q^3(II) sites exhibit lower degrees of hydration at all the conditions used.

Table 3
Relative integral areas extracted from the deconvoluted ^{1}H—^{29}Si CPMAS NMR spectra (B_0 = 11.7 T, ν_R = 12.5 kHz) with Hartmann-Hahn contact periods of t = 2 and 8 ms. δ_{iso} and FWHM were required to be consistent in the ^{1}H—^{29}Si MAS NMR spectra acquired with Hartmann-Hahn contact periods of t = 2 and 8 ms.

Curing time (days)	Contact time (ms)	Relative integral area (%)[a]				
		Q^1	Q^2	Q^3(I)	Q^3(II)	Q^4
56	2	10 %	30 %	57 %	3 %	0 %
	8	10 %	22 %	61 %	7 %	0 %
	Difference[b]	0 %	−8 %	4 %	4 %	0 %
112	2	8 %	28 %	57 %	8 %	0 %
	8	3 %	22 %	63 %	12 %	0 %
	Difference[b]	−5 %	−6 %	6 %	4 %	0 %

[a] The relative integrated intensity for each resonance is normalised to the sum of all sites within the sample and is obtained by simulating the ^{1}H—^{29}Si CPMAS NMR spectra. Estimated error in the relative integral area is 1 %.
[b] The difference for each site is calculated by comparing the data for t = 8 ms and t = 2 ms.

A comparison of the changes in the relative integral areas shown in 3.4 (the difference between t = 2 and 8 ms) show that in the M-S-H gel cured for 56 days Q^3(I) and Q^3(II) sites exhibit similar degrees of local hydration. Additionally, this quantification shows that Q^2 sites exhibit a greater degree of local hydration than the Q^1 sites. Given that Q^2 and Q^1 sites comprise two and three hydroxyl groups, respectively, the differences observed cannot solely result from differences in polymerisation. The data therefore indicate clustering of water molecules around Q^2 sites within the silicate chains of M-S-H, with less water molecules surrounding Q^1 sites at the end of these silicate chains.

Regarding the samples cured for 112 days, the less abundant Q^3(II) site has a greater degree of local hydration than the more abundant Q^3(I) site, as suggested by the comparison between the changes in the relative integral areas at t = 2 and 8 ms, respectively. As each of these Q^3 sites comprises a central Si atom in tetrahedral coordination linked to three other tetrahedral Si atoms (via oxygen bridges) and a hydroxyl group, the difference in the degree of local hydration cannot result from differences in the extent of polymerisation. Therefore, the ^{1}H—^{29}Si CPMAS NMR indicates some degree of preferential arrangement of water molecules around the lower abundance Q^3(II) site. The data also shows that Q^2 and Q^1 sites in the M-S-H gel exhibit similar degrees of local hydration after 112 days of curing.

Together, a comparison of the changes in the relative integral areas of each resonance in the ^{1}H—^{29}Si CPMAS NMR data indicates that the

Table 4
Summary of the evolution of Mg and Si within the forming M-S-H throughout the curing period investigated.

Curing time (d)	Mg reacted[a] (mol·100 g^{-1})	Si reacted[b] (mol·100 g^{-1})	Extent Mg (α)	Extent Si (α)
0	0.00	0.00	0.00	0.00
7	0.10	0.02	0.12	0.02
14	0.13	0.10	0.17	0.13
28	0.28	0.30	0.36	0.40
56	0.60	0.64	0.85	0.95
112	0.69	0.63	1.00	0.96

[a] Obtained from TG data.
[b] Obtained from ^{29}Si MAS NMR data (Q^4 sites).

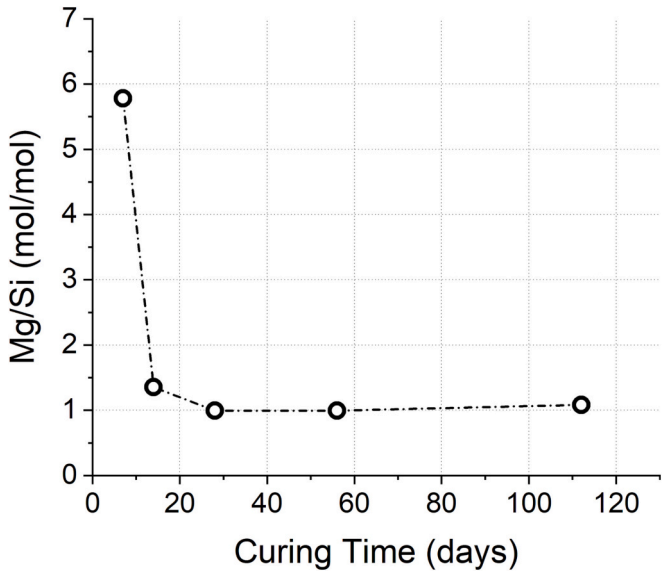

Fig. 11. Evolution of the Mg/Si molar ratio within the precipitated M-S-H gel.

rearrangement in the local hydration of each site continue to occur with time even after complete dissolution of Si sites in silica fume and incorporation of Si into the M-S-H. In fact, water molecules that are initially evenly distributed across both Q^3(I) and Q^3(II) sites at 56 days of curing become clustered around Q^3(II) sites after 112 days, and water molecules initially clustered around Q^2 sites at 56 days are more evenly distributed across both Q^2 and Q^1 sites after 112 days. Overall, in the M-S-H gel cured for 56 days, water molecules are primarily clustered around low polymerisation Q^2 sites within the silicate chains, and in the M-S-H gel cured for 112 days, water molecules are primarily clustered around low polymerisation Q^2 and Q^1 sites.

3.4. Reaction kinetics and mechanism of M-S-H formation

The outcomes gained by investigations of the reaction of brucite and silica fume, and subsequent formation of M-S-H, were here combined to discuss the evolution of the equilibrium between Mg and Si within the M-S-H gel over time. Data for this was obtained from the TG and NMR data for Mg and Si, respectively; specifically, the Mg remaining as Mg $(OH)_2$ was obtained from the wt% of $Mg(OH)_2$ obtained via TG, while the amount of Si remaining as SiO_2 was obtained from the quantification of Q^4 Si sites in the NMR data. The amount of Mg and Si within the M-S-H was reliably calculated by difference between the initial (weighed) and final elemental partitioning within the unreacted brucite and silica fume. No additional phases could be detected through XRD, TG, or NMR analysis. The extent of reaction, α, was calculated for both Mg and Si, reflecting the portion of brucite and silica fume hydrated, respectively. All the information related to this is reported in Table 4 below, with Mg and Si expressed as mol per 100 g of solids.

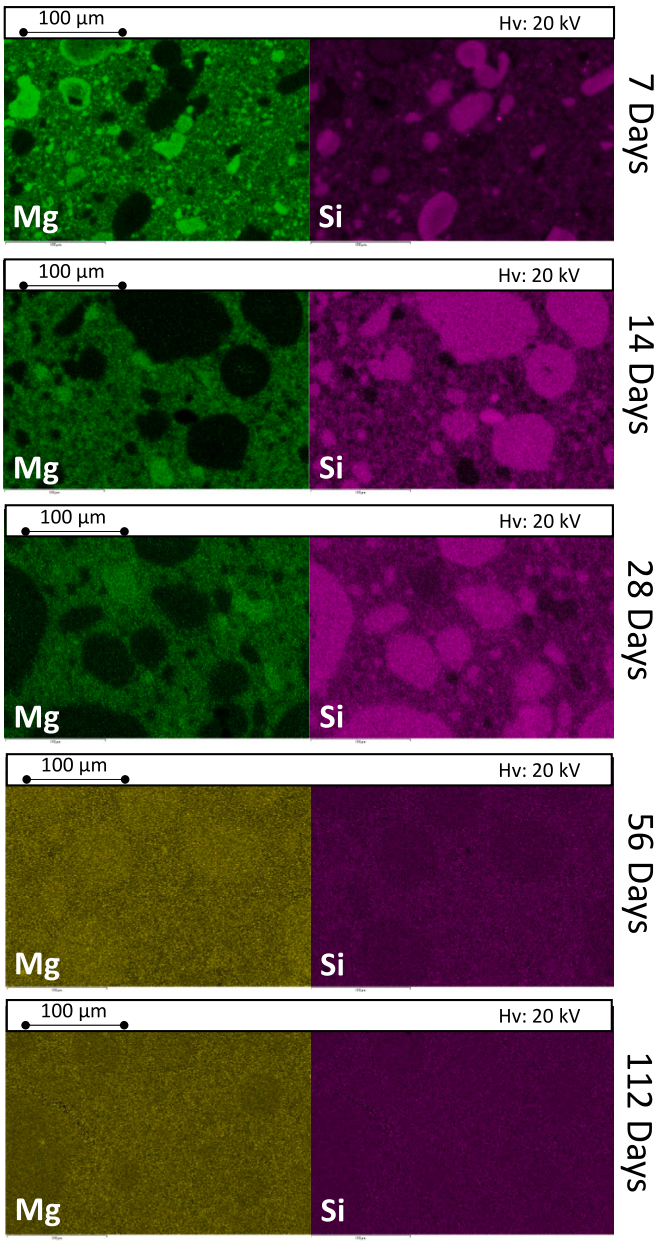

Fig. 12. Spatially-resolved SEM-EDX analysis for all the curing ages investigated, with elemental detection (wt%) of Mg (green/yellow) and Si (purple); all the analyses have been conducted at a magnification, working distance and voltage of 1000, 8.5 mm and 20 kV, respectively. (For interpretation of the references to colour in this figure legend, the reader is referred to the web version of this article.)

As shown, the reaction of Si was initially slower than that of Mg, reflecting initially lower kinetics of dissolution; however, almost all silica fume (95 mol%) appeared to have reacted after 56 days of curing, whereas brucite was completely dissolved only after 112. Based on the Mg and Si reacted, the Mg/Si ratio of the M-S-H at each curing period was estimated as shown in Fig. 11.

Reflecting the slow reaction of Si at the earlier stage, the Mg/Si ratio is initially very high, but decreases to and remains at 0.93 in 28–56 days. The Mg/Si ratio increases to 1.08 at 112 days, when the reaction of Si stops but Mg continues to react, which coincides with the initial Mg/Si ratio of 1.05.

The outcomes merged from XRD, TG, and NMR analyses were confirmed through the spatially resolved chemical composition data

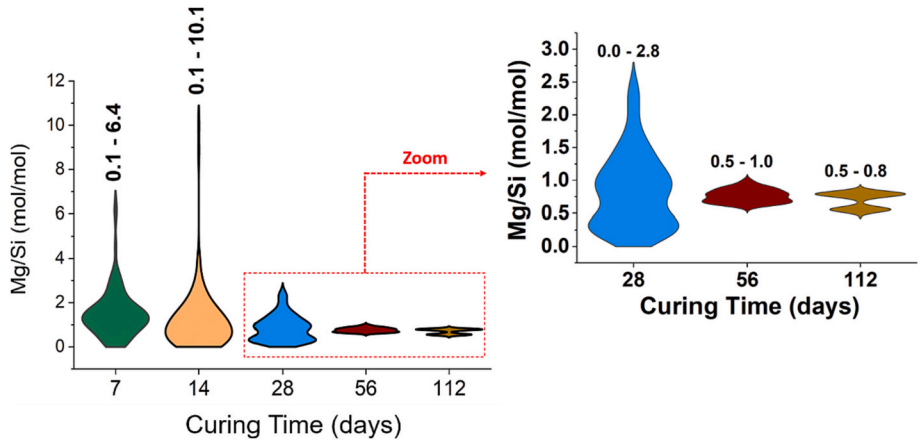

Fig. 13. Mg/Si molar ratio distribution plots, plotted from data obtained by SEM-EDX. Data were obtained via EDX point analysis of evenly distributed points across a representative 250 μm × 250 μm section of the sample. A total of 100 individual points were collected per sample at each age. For each curing age assessed, the width of the distribution at each plotted Mg/Si molar ratio value indicates the relative proportion of points on the sample section exhibiting that Mg/Si molar ratio value.

gained from SEM-EDX analysis of the M-S-H samples cured for different time periods. The outcomes are shown in Fig. 12, where the elemental detection of Mg and Si is highlighted in green/yellow and purple, respectively.

The backscattered electron (BSE) image, and associated EDX maps, for the M-S-H sample cured for 7 days shows the presence of unreacted particles of silica fume and brucite embedded within a dense M-S-H gel. At longer curing ages (14 and 28 days), the enhanced dissolution of silica fume and brucite could be observed through the reduced resolution of the boundaries of the reactant particles (i.e. the boundaries became less defined, due to reaction of these constituents). Specifically, high-intensity signals for both Mg and Si in silica fume and brucite could still be observed after 7 days of curing, embedded within a homogenous distribution of Mg and Si signals due to the formation of M-S-H gel. As discussed above, the chemical composition of the M-S-H gel was expected to vary somewhat for samples cured for longer than 28 days, and this was confirmed by the EDX analysis.

The SEM-EDX data (Fig. 13) identified the formation of two M-S-H gels with distinct chemical compositions after 112 days curing: a Si-rich M-S-H gel with molar Mg/Si = 0.55 (±0.2), and a Mg-rich M-S-H gel with molar Mg/Si = 0.80 (±0.5). The SEM-EDX data indicate that the Si-rich M-S-H gel was forming within regions of the sample where silica fume particles originally existed, and hence more Si was available. Hence, it is likely that the early-stage (up to 28 days) formation of M-S-H in proximity of the silica fume particles leads to decreasing kinetics of silica fume dissolution, limiting the mass transport of Si away from Si fume particles. On the contrary, the Mg-rich M-S-H gel forms within the regions more distant from where particles of silica fume originally existed, and consistent with the significantly faster reaction of brucite, when compared to silica fume, that was observed by XRD, TG and NMR. However, the Mg/Si molar ratio appeared highly disordered up to 28 days of curing, reflecting the early-stage evolution of M-S-H (Fig. 13).

This observation was likely due to inhomogeneous mixing and incongruent dissolution of brucite and silica fume particles. The scattering significantly lowered between 28 and 56 days of curing, when Mg/Si molar ratios between 0.5 and 1 were registered. As previously discussed from NMR data, the M-S-H continued to evolve in terms of both chemical composition and nanostructure, and after 112 days of curing the average Mg/Si ratio slightly increased to 0.8–1.0. This suggests that the slow dissolution of brucite led to an unstable M-S-H gel with varying Mg/Si ratios until the full availability of Mg^{2+} ions could be achieved, beyond 56 days of curing (Fig. 4A). However, it was calculated from 100 EDX data points per BSE image that 1.5 mol of Mg-rich M-S-H gel was formed for every mole of Si-rich M-S-H gel. The SEM/EDX analysis confirmed the achievement of the plateaus in terms of silica fume dissolution and incorporation of Si within the M-S-H, originally identified in the analysis of the ^{29}Si MAS NMR data (Fig. 9); in fact, Si-rich regions could clearly be distinguished after 56 and 112 days of hydration (Fig. 12). An ordinary one-way ANOVA analysis of the EDX data for samples cured for 28, 56, and 112 days showed that the mean Mg/Si ratio of the M-S-H gels decreased over time ($p = 0.0036$). The greatest change in the mean Mg/Si ratio of the M-S-H gels occurred between 28 and 56 days (mean Mg/Si = 0.85 at 28 days compared with mean Mg/Si = 0.77 at 56 days) ($p = 0.0267$), which continued to 112 days (mean Mg/Si = 0.70), but with no significant change occurring between 56 and 112 days ($p = 0.8182$).

The mechanisms and kinetics of dissolution of SiO_2 and $Mg(OH)_2$ to form M-S-H was analysed using three solid-state kinetic models often used for solid state reactions [55], specifically the Avrami-Erofeyey nucleation model, the contracting volume model, and the 3D diffusion model (Eqs. (1), (2), and (3), respectively).

$$[-ln(\mathbf{1}-\boldsymbol{\alpha})]^{1/n} = \mathbf{kt} \quad (1)$$

$$\mathbf{1}-(\mathbf{1}-\boldsymbol{\alpha})^{1/3} = \mathbf{kt} \quad (2)$$

$$\left[\mathbf{1}-(\mathbf{1}-\boldsymbol{\alpha})^{1/3}\right]^2 = \mathbf{kt} \quad (3)$$

Eq. (1) describes the Avrami-Erofeyey nucleation model, accounting for the formation and growth of a nucleation site via coalescence with other nucleation sites, and the resulting loss of reactant-product interface due to the merger of reaction zones of two or more growing nuclei; Eq. (2) describes the contracting volume model, which assumes the volume reduction of a spherical reactant and the associated reduction in reactant-product interface; and Eq. (3) describes the contracting 3D diffusion model, according to which the formation of a product surface layer hinders the further movement of the reactants towards the reaction interface or products from the reaction interface. The extents of reaction $\boldsymbol{\alpha}$ reported in Table 4 for both silica fume and brucite were inserted into Eqs. (1), (2), and (3), and the outcomes reported in Figs. 14A, B, and C, respectively, showing the quality of the fit to the data produced by each model for the individual phase considered. For the purpose of fitting, Eq. (1) (Avrami-Erofeyey nucleation model) was rearranged to give Eq. (4):

$$ln[-ln(\mathbf{1}-\boldsymbol{\alpha})] = \mathbf{nln(k)} + \mathbf{nln(t)} \quad (4)$$

Overall, the nucleation model (Eq. (1)) appeared to better fit the experimental data reported in Table 4, and therefore it was used to

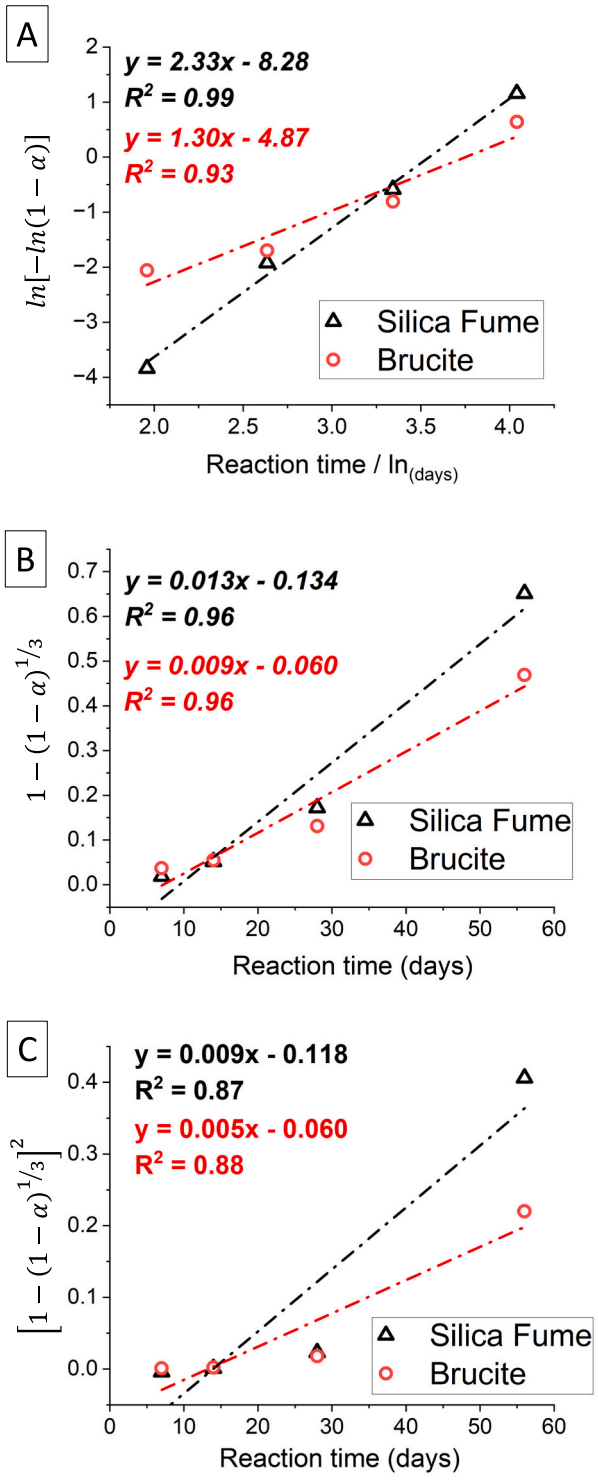

Fig. 14. Fitting of the extent of reaction (α) for silica fume and brucite up to 56 days: (A) nucleation model, (B) contracting volume model, (C) contracting 3D diffusion model [55].

calculate the parameters n and k, separately for silica fume and brucite; for both phases, the data up to 56 days was considered, since the dissolution could be considered negligible beyond that (Table 4). Regarding the dissolution of silica fume, the Avrami-Erofeyev model clearly was the best fit to the experimental data ($R^2 = 0.99$). Since only M-S-H is forming in the system, the parameters n and k of 2.33 and 0.029 were likely suggesting that the precipitation of M-S-H was not a linear function of the concentration of the reactants, and that the kinetics of reaction were dependent on several other factors. Likely, the nucleation and growth of M-S-H was the rate-limiting factor for the reaction.

Similar analysis for $Mg(OH)_2$ consumption also showed a good correlation with the models considered, with the contracting volume model (Eq. (2)) reflecting the best fit ($R^2 = 0.96$, Fig. 14B). However, the data for $Mg(OH)_2$ also showed good correlation ($R^2 = 0.93$) with the Avramy-Erofeyev model (Eq. (1)), and this was considered to calculate the n (1.30) and k (0.236) parameters for $Mg(OH)_2$, as it was reported for silica fume above. The slightly lower n value gained for Mg was likely due to the faster initial dissolution of brucite, which appeared to follow a nearly linear trend throughout the curing time investigated.

4. Conclusions

M-S-H gels were synthesised via reaction of $Mg(OH)_2$ with silica fume, and ^{25}Mg and ^{29}Si MAS NMR and $^{1}H—^{29}Si$ CP MAS NMR spectroscopy experiments, complemented by X-ray diffraction, electron microscopy, and thermogravimetric measurements, were used to examine and quantify 1) the dissolution of brucite and silica fume during reaction, 2) the chemical and nanostructural evolution of the M-S-H gels over time, and 3) model the reaction kinetics and mechanism of M-S-H formation.

The novelty of this work lies primarily in 1) the use of $Mg(OH)_2$ as a precursor (which mitigates to some extent the scarcity of natural $MgCO_3$ used to produced MgO), 2) the combination of advanced microstructural, thermal, and spectroscopic analytical techniques to acquire novel data regarding reaction mechanisms, kinetics, and evolution of gel chemical composition and nanostructure, and 3) quantification and subsequent fitting of the extent of reaction (calculated using the aforementioned data) to show that M-S-H formation in these samples is described by the Avrami-Erofeyev nucleation model.

In each sample, a M-S-H gel was formed after curing for 7 days, with no additional reaction products observed at any curing age examined (up to 112 days). The M-S-H gel exhibited a microstructure with a gel-like morphology, with globular chains. During the early stages of reaction (<56 days curing), the gels exhibited significant variations in chemical composition (with a broad distribution of molar Mg/Si values of between 0.5 and 1.0), however after curing for 112 days, two distinct M-S-H gels were formed, each with minimal variation in chemical composition: a Si-rich M-S-H gel with molar Mg/Si = 0.55 (±0.2), and a Mg-rich M-S-H gel with molar Mg/Si = 0.80 (±0.5). This appeared to result from the spatial distribution of silica fume and brucite particles, which caused kinetic limitations on mass transport of Si and Mg ions, creating regions rich in either Si or Mg ions.

For all samples, multinuclear solid-state NMR spectroscopy experiments probing ^{25}Mg and ^{29}Si nuclei, including measurements at high field, showed unambiguously the formation of a M-S-H gel with structural similarity to the thermodynamically stable serpentine-group mineral lizardite, suggesting that a thermodynamically stable M-S-H is formed within 112 days in these samples. The M-S-H gel at each curing time exhibited a high degree of Q^3 Si sites relative to Q^2 and Q^1 Si sites, indicating a significant degree of polymerisation. After 56 days curing, ^{25}Mg and ^{29}Si MAS NMR and $^{1}H—^{29}Si$ CP MAS NMR spectroscopy and SEM-EDX data showed continued incorporation of Mg into the M-S-H gel and subsequent preferential formation of the Mg-rich M-S-H phase in the sample.

Quantification of data from ^{25}Mg and ^{29}Si MAS NMR and $^{1}H—^{29}Si$ CP MAS NMR spectroscopy experiments, electron microscopy, and thermogravimetric measurements showed that upon mixing of brucite, silica fume, and water, dissolution of brucite and silica fume both occurred approximately linearly with time up to 56 days curing, correlating with the subsequent formation of M-S-H that occurred approximately linearly with time up to 56 days. The data were fit with and showed strong correlation with the Avrami-Erofeyev nucleation solid-state kinetic model, indicating that the mechanism behind the formation of M-S-H in

these samples was governed by nucleation reactions.

After this time, the consumption of silica fume and brucite and their incorporation of Si and Mg into M-S-H plateaus, but the nanostructural rearrangement of the M-S-H gel continues, with an increase in cross-linking and polymerisation of M-S-H as the gel ages. Furthermore, rearrangement in the local hydration (i.e. clustering of water molecules) surrounding each Si site occurs as the gel age, with M-S-H silicate chains becoming more hydrated than the endmembers or crosslinking members.

Through quantification of the thermogravimetric and NMR data and associated spectral deconvolutions, and fitting data regarding dissolution and extent of reaction over time with the appropriate solid-state kinetic models, this study reveals mechanisms and kinetics of M-S-H formation, and the chemical composition, nanostructure, and local hydration of these M-S-H gels. This has significant implications for the application of binders comprising M-S-H gels in construction and contaminant and radioactive waste immobilisation applications, particular regarding chemical durability and immobilisation capability.

Furthermore, this study highlighted the limitations of using solely XRD data to identify formation of M-S-H gels, and the necessary use of both spectroscopic and thermogravimetric characterisation techniques to identify and quantify this phase conclusively, as we have done here. Further work is also recommended to explore the reaction mechanisms, kinetics, and nanostructural evolution of M-S-H gels produced using different proportions of reactants to those used here. This would provide further understanding of the effect of precursor chemistry on M-S-H gel reaction and characteristics.

Declaration of competing interest

The authors declare that they have no competing interests, or other interests that might be perceived to influence the interpretation of the article.

Data availability

Data will be made available on request.

Acknowledgements

This work was supported by the Engineering and Physical Science Research Council (EPSRC grant EP/R025959/1). This research also utilised the HADES/MIDAS facility at the University of Sheffield established with financial support from EPSRC and BEIS (grant EP/T011424/1). The UK 850 MHz solid-state NMR Facility used in this research was funded by EPSRC and BBSRC (grant EP/T015063/1), as well as the University of Warwick including via part funding through Birmingham Science City Advanced Materials Projects 1 and 2 supported by Advantage West Midlands (AWM) and the European Regional Development Fund (ERDF). We wish to thank Dr. Sandra van Meurs, Department of Chemistry, The University of Sheffield, for assistance in acquiring the ^{29}Si NMR data and insightful discussions related to this work.

Appendix A. Supplementary data

Supplementary data to this article can be found online at https://doi.org/10.1016/j.cemconres.2023.107295.

References

[1] E. Gartner, T. Sui, Alternative cement clinkers, Cem. Concr. Res. 114 (2018) 27–39.
[2] S.A. Walling, J.L. Provis, Magnesia-based cements: a journey of 150 years, and cements for the future? Chem. Rev. 116 (7) (2016) 4170–4204.
[3] B. Wang, C. Fan, Hydration behavior and immobilization mechanism of MgO–SiO2–H2O cementitious system blended with MSWI fly ash, Chemosphere 250 (2020), 126269.
[4] N.C. Collier, N.B. Milestone, The encapsulation of Mg (OH) 2 sludge in composite cement, Cem. Concr. Res. 40 (3) (2010) 452–459.
[5] A. Violante, et al., Mobility and bioavailability of heavy metals and metalloids in soil environments, J. Soil Sci. Plant Nutr. 10 (3) (2010) 268–292.
[6] J.G. MacGregor, et al., Reinforced Concrete: Mechanics and Design 3, Prentice Hall, New Jersey, 1997.
[7] S. Zuo, et al., Rheological behaviour of low-heat Portland cement paste with MgO-based expansive agent and shrinkage reducing admixture, Constr. Build. Mater. 304 (2021), 124583.
[8] U.S.G. Survey, Magnesium compounds. Mineral Commodity Summaries 2015 (2015) 96–97.
[9] S. Madeddu, et al., Alkaline digestion of dunite for Mg (OH) 2 production: an investigation for indirect CO2 sequestration, Miner. Eng. 59 (2014) 31–38.
[10] S. Madeddu, et al., Extraction of Mg (OH) 2 from Mg silicate minerals with NaOH assisted with H2O: implications for CO2 capture from exhaust flue gas, Faraday Discuss. 183 (2015) 369–387.
[11] J.M. Gieskes, G. Peretsman, P. Rabinowitz, Water chemistry procedures aboard JOIDES resolution—some comments, ODP Tech. Note 5 (1986) 1–46.
[12] F. Schorcht, et al., Best Available Techniques (BAT) Reference Document for the Production of Cement, Lime and Magnesium Oxide, European Commission Joint Research Centre Institute for Prospective Technological Studies, Luxembourg, 2013.
[13] S.A. Walling, et al., Structure and properties of binder gels formed in the system Mg (OH) 2–SiO 2–H 2 O for immobilisation of Magnox sludge, Dalton Trans. 44 (17) (2015) 8126–8137.
[14] B. Lothenbach, et al., Magnesium and calcium silicate hydrates, Cem. Concr. Res. 77 (2015) 60–68.
[15] D. Bonen, Composition and appearance of magnesium silicate hydrate and its relation to deterioration of cement-based materials, J. Am. Ceram. Soc. 75 (10) (1992) 2904–2906.
[16] D.R.M. Brew, F.P. Glasser, Synthesis and characterisation of magnesium silicate hydrate gels, Cem. Concr. Res. 35 (1) (2005) 85–98.
[17] E. Bernard, et al., Characterization of magnesium silicate hydrate (MSH), Cem. Concr. Res. 116 (2019) 309–330.
[18] C. Roosz, et al., Crystal structure of magnesium silicate hydrates (MSH): the relation with 2: 1 Mg–Si phyllosilicates, Cem. Concr. Res. 73 (2015) 228–237.
[19] B. Walkley, J.L. Provis, Solid-state nuclear magnetic resonance spectroscopy of cements, Mater. Today Adv. 1 (2019), 100007.
[20] S.A. Walling, et al., Structure and properties of binder gels formed in the system Mg $(OH)_2$–SiO_2–H_2O for immobilisation of Magnox sludge, Dalton Trans. 44 (17) (2015) 8126–8137.
[21] M. Tonelli, et al., Structural characterization of magnesium silicate hydrate: towards the design of eco-sustainable cements, Dalton Trans. 45 (8) (2016) 3294–3304.
[22] E. Bernard, et al., Formation of magnesium silicate hydrates (MSH), Phys. Chem. Earth A/B/C 99 (2017) 142–157.
[23] H. Zhao, et al., Acceleration of MSH gel formation through the addition of alkali carbonates, in: 15th International Congress on the Chemistry of Cement, 2019. Sheffield.
[24] D. Massiot, et al., Modelling one- and two-dimensional solid-state NMR spectra, Magn. Reson. Chem. 40 (1) (2002) 70–76.
[25] D. Iuga, A.P.M. Kentgens, Influencing the satellite transitions of half-integer quadrupolar nuclei for the enhancement of magic angle spinning spectra, J. Magn. Reson. 158 (1) (2002) 65–72.
[26] D. Freude, J. Haase, in: H. Pfeifer, P. Barker (Eds.), Quadrupole Effects in Solid-State Nuclear Magnetic Resonance, in Special Applications, Springer Berlin Heidelberg, Berlin, Heidelberg, 1993, pp. 1–90.
[27] T. Zhang, L.J. Vandeperre, C.R. Cheeseman, Formation of magnesium silicate hydrate (MSH) cement pastes using sodium hexametaphosphate, Cem. Concr. Res. 65 (2014) 8–14.
[28] J. Temuujin, K. Okada, K.J.D. MacKenzie, Role of water in the mechanochemical reactions of MgO–SiO2Systems, J. Solid State Chem. 138 (1) (1998) 169–177.
[29] D. Nied, et al., Properties of magnesium silicate hydrates (MSH), Cem. Concr. Res. 79 (2016) 323–332.
[30] A. Dauzeres, et al., Magnesium perturbation in low-pH concretes placed in clayey environment—solid characterizations and modeling, Cem. Concr. Res. 79 (2016) 137–150.
[31] M.J. McKelvy, et al., Magnesium hydroxide dehydroxylation: in situ nanoscale observations of lamellar nucleation and growth, Chem. Mater. 13 (3) (2001) 921–926.
[32] K. Nahdi, F. Rouquerol, M.T. Ayadi, Mg (OH) 2 dehydroxylation: a kinetic study by controlled rate thermal analysis (CRTA), Solid State Sci. 11 (5) (2009) 1028–1034.
[33] T. Mitsuda, H. Taguchi, Formation of magnesium silicate hydrate and its crystallization to talc, Cem. Concr. Res. 7 (3) (1977) 223–230.
[34] F. Jin, A. Al-Tabbaa, Thermogravimetric study on the hydration of reactive magnesia and silica mixture at room temperature, Thermochim. Acta 566 (2013) 162–168.
[35] A. Dumas, et al., Phyllosilicates synthesis: a way of accessing edges contributions in NMR and FTIR spectroscopies. Example of synthetic talc, Phys. Chem. Miner. 40 (4) (2013) 361–373.
[36] J. Wei, et al., Reaction products of MgO and microsilica cementitious materials at different temperatures, J. Wuhan Univ. Technol. Mate. Sci. Edit. 26 (4) (2011) 745–748.
[37] J. Temuujin, K. Okada, K.J. MacKenzie, Formation of layered magnesium silicate during the aging of magnesium hydroxide–silica mixtures, J. Am. Ceram. Soc. 81 (3) (1998) 754–756.

[38] J.-B. d'Espinose de la Caillerie, M. Kermarec, O. Clause, ^{29}Si NMR observation of an amorphous magnesium silicate formed during impregnation of silica with Mg (II) in aqueous solution, J. Phys. Chem. 99 (47) (1995) 17273–17281.
[39] A. Pedone, F. Palazzetti, V. Barone, Models of aged magnesium–silicate–hydrate cements based on the lizardite and talc crystals: a periodic DFT-GIPAW investigation, J. Phys. Chem. C 121 (13) (2017) 7319–7330.
[40] A.C.A. Muller, et al., Influence of silica fume on the microstructure of cement pastes: new insights from ^{1}H NMR relaxometry, Cem. Concr. Res. 74 (2015) 116–125.
[41] H. Hilbig, F.H. Köhler, P. Schießl, Quantitative ^{29}Si MAS NMR spectroscopy of cement and silica fume containing paramagnetic impurities, Cem. Concr. Res. 36 (2) (2006) 326–329.
[42] X.J. Wang, et al., ^{29}Si NMR characterization of silica tetrahedron in the silica fume simulate hydration, Key Eng. Mater. 539 (2013) 1–4.
[43] K. MacKenzie, R. Meinhold, Thermal reactions of chrysotile revisited: a ^{29}Si and ^{25}Mg MAS NMR study, Am. Mineral. 79 (1–2) (1994) 43–50.
[44] K. Kosuge, K. Shimada, A. Tsunashima, Micropore formation by acid treatment of antigorite, Chem. Mater. 7 (12) (1995) 2241–2246.
[45] Nakata, S.-I., et al., Characterization of natural zeolites and clay minerals by high-resolution solid-state NMR. J. Clay Sci. Soc. Japan (in Japanese), 1986. 26(3): p. 197–208.
[46] K. MacKenzie, R. Meinhold, The thermal reactions of talc studied by ^{29}Si and ^{25}Mg MAS NMR, Thermochim. Acta 244 (1994) 195–203.
[47] G. Webb, C.P. Slichter, Principles of Magnetic Resonance. Springer Series in Solid-State Sciences, Vol. by M. Cardoua, P. Fulde and HJ Queisser, Springer-Verlag, Berlin, 1978, 397 pages. DM 54, US $27.00. Organic Magnetic Resonance, 1979. 12(3): p. IV-IV.
[48] P.J. Pallister, I.L. Moudrakovski, J.A. Ripmeester, Mg-25 ultra-high field solid state NMR spectroscopy and first principles calculations of magnesium compounds, Phys. Chem. Chem. Phys. 11 (48) (2009) 11487–11500.
[49] P.S. Fiske, J.F. Stebbins, I. Farnan, Bonding and dynamical phenomena in MgO: a high temperature ^{17}O and ^{25}Mg NMR study, Phys. Chem. Miner. 20 (8) (1994) 587–593.
[50] T. Bastow, 25Mg nuclear quadrupole coupling in mg (OH) 2, Solid State Commun. 77 (7) (1991) 547–548.
[51] M. Vespa, et al., Characterisation of magnesium silicate hydrate phases (M-S-H): a combined approach using synchrotron-based absorption-spectroscopy and ab initio calculations, Cem. Concr. Res. 109 (2018) 175–183.
[52] E. Bernard, et al., Magnesium and calcium silicate hydrates, part I: investigation of the possible magnesium incorporation in calcium silicate hydrate (C-S-H) and of the calcium in magnesium silicate hydrate (M-S-H), Appl. Geochem. 89 (2018) 229–242.
[53] B.W. Evans, The Serpentinite multisystem revisited: chrysotile is metastable, Int. Geol. Rev. 46 (6) (2004) 479–506.
[54] E.K. Peters, D-18O enriched waters of the Coast Range Mountains, northern California: connate and ore-forming fluids, Geochim. Cosmochim. Acta 57 (5) (1993) 1093–1104.
[55] A. Khawam, D.R. Flanagan, Solid-state kinetic models: basics and mathematical fundamentals, J. Phys. Chem. B 110 (35) (2006) 17315–17328.